



# Numerical analyses of the solubility trapping of CO<sub>2</sub> storage in geological formations



Qingliang Meng<sup>a</sup>, Xi Jiang<sup>a,b,\*</sup>

<sup>a</sup> Department of Safety Science Engineering & State Key Laboratory of Fire Science, University of Science and Technology of China, Hefei, Anhui 230026, China

<sup>b</sup> Engineering Department, Lancaster University, Lancaster LA1 4YR, United Kingdom

## HIGHLIGHTS

- CO<sub>2</sub> solubility trapping in saline aquifers with horizontal and inclined caprocks is numerically studied.
- Several differences between the 2D and 3D results are observed.
- 3D effects could be important in the convective period but negligible for predicting the onset of convection.
- The solubility trapping shows directional dependence for the inclined caprock surfaces.

## ARTICLE INFO

### Article history:

Received 23 September 2013

Received in revised form 10 January 2014

Accepted 13 January 2014

Available online 6 February 2014

### Keywords:

Carbon storage  
Geological formation  
Numerical simulation  
Solubility trapping  
Density driven fingering

## ABSTRACT

Numerical analyses are performed to study the fluid dynamic behaviours of the solubility trapping in the context of CO<sub>2</sub> storage in deep geological formations. Dissolution of CO<sub>2</sub> into the underlying brine increases the density of brine, leading to a gravitational instability. This instability could give rise to the fingering of CO<sub>2</sub>-rich brine, which would trigger fluid convection and greatly enhance the dissolution rate of CO<sub>2</sub>. In light of understanding the three-dimensional (3D) effects on the process as well as the effects of caprock slope, both two-dimensional (2D) and 3D simulations are carried out in this study. For the case with no slope, several differences between the 2D and 3D results are observed in the mass transfer process including the CO<sub>2</sub> dissolving rate, although the differences between the results are not obvious at the early stages. The analyses of the 3D results with different grid resolutions show that 3D effects could be important in the convective period while they might be negligible in predicting the onset of convection. For the inclined case, the number of fingers is reduced and the interaction of fingers is weakened with the increase of the inclined angle. The results of inclined cases show a clear directional dependence, indicating that 2D simulations cannot be used for the prediction of the solubility trapping when the caprock has an inclined surface.

© 2014 Elsevier Ltd. All rights reserved.

## 1. Introduction

Carbon dioxide (CO<sub>2</sub>) storage in deep geological formations is potentially the most promising method for massively reducing the greenhouse gas emissions from fossil fuel combustion into the atmosphere [1,2]. In this method, one of the primary mechanisms of securing CO<sub>2</sub> at the underground conditions is that the low-permeability caprock will prevent the injected CO<sub>2</sub> from leaking to the surface and CO<sub>2</sub> would diffuse in the permeable, porous zone for an extended period of time (i.e. static trapping) [2]. At the temperature and pressure conditions of deep brine formations (for temperature higher than 31.1 °C and pressure higher than 7.39 MPa [2]), the injected CO<sub>2</sub> will be in a supercritical state

(scCO<sub>2</sub>). Since the density of scCO<sub>2</sub> is lower than that of the native aqueous phase, it will tend to accumulate at the top of reservoir and spread out along the top caprock [1,2], as schematically shown in Fig. 1(a). In addition to static trapping that impedes CO<sub>2</sub> flowing upward, other trapping mechanisms such as solubility trapping and mineral trapping should either immobilize the CO<sub>2</sub> or eliminate its upward buoyant movement, to ensure the safe storage of CO<sub>2</sub> over long time scales [2].

Solubility trapping occurs when the injected CO<sub>2</sub> is transported by molecular diffusion away from the interface between the gas-aqueous two-phase zone above and the single aqueous phase zone below, and then dissolves into the underlying aqueous phase [3], which will increase the density of the aqueous phase by 0.1–1%, depending on the salinity of brine [4,5]. The density increase can induce a gravitational instability [6]. When the small instability grows, a pattern of the dissolved CO<sub>2</sub> concentration that looks like fingers would form, referring to as density-driven “fingering”. This

\* Corresponding author at: Engineering Department, Lancaster University, Lancaster LA1 4YR, United Kingdom. Tel.: +44 1524 592439; fax: +44 1524 381707.  
E-mail address: [x.jiang@lancaster.ac.uk](mailto:x.jiang@lancaster.ac.uk) (X. Jiang).

## Nomenclature

### Abbreviation

*Ra* Rayleigh number

### Symbols

*D* diffusivity of CO<sub>2</sub> in brine  
*D*<sub>1</sub> distance from mesh *m* to the interface between meshes *m* and *n*  
*D*<sub>2</sub> distance from mesh *n* to the interface between meshes *m* and *n*  
*D*<sub>mn</sub> distance from mesh *n* to mesh *m*  
 $\mathbf{g}$  gravitational acceleration  
*K* permeability  
*M*<sub>CO<sub>2</sub></sub> molar mass of CO<sub>2</sub>  
 $\mathbf{n}$  surface normal vector  
*P* pressure  
 $\mathbf{q}$  Darcy flux  
*S* surface area of connected mesh interface  
*t* time  
*T* temperature

*V* mesh volume  
*V*<sub>φ</sub> partial molar volume  
*X*<sub>0</sub> concentration at the top boundary  
*X*<sub>*i*</sub> mass fraction of component *i*  
*X*<sub>s</sub> salinity  
*X, Y, Z* Cartesian coordinates  
 $\alpha$  intersection angle  
 $\delta_c$  critical thickness of diffusive boundary layer  
 $\lambda_c$  critical wavelength  
 $\mu$  dynamic viscosity of brine  
 $\rho$  density of the aqueous phase  
 $\rho_i$  partial density of component *i*  
 $\phi$  porosity of the formations  
 $\nabla$  gradient operator

### Subscripts/superscripts

*i* (*i* = 1, brine; *i* = 2, CO<sub>2</sub>)  
*c* critical

phenomenon will result in fluid convection, in which denser CO<sub>2</sub>-rich aqueous fluids will be transported downward while less dense fluids will flow upward [7]. It is known that this mechanism could significantly accelerate the dissolving rate of CO<sub>2</sub> and improve CO<sub>2</sub> geological storage security [3,6–10].

Because of the importance of solubility trapping to CO<sub>2</sub> geological storage, the process has been the focus of research by a number of theoretical, experimental, and numerical studies. For example, Lindeberg and Wessel-Berg [11] undertook a theoretical analysis to examine under what conditions natural vertical convection might occur after CO<sub>2</sub> is injected into a deep aquifer, followed by several linear stability analyses for the onset time of convection using different theoretical approaches [6,9,10,12–15]. Several important relations for the prediction of critical time and associated unstable behaviours were obtained in isotropic and anisotropic media. However, the linear stability analyses can only be used to determine the critical onset behaviours of convection and cannot be used to characterise the convection mechanism after the onset of convection. To complement the theoretical analyses, comprehensive experimental studies, e.g. [16–21], as well as numerical simulations, e.g. [3,6,7,9,10,12,22–25], were also carried out to investigate the qualitative and quantitative aspects of this process. For example, it was found that convective transport rate was almost two orders of magnitude larger than the pure diffusive

rate of CO<sub>2</sub> in water or similar reservoir brines [18]. Although experimental studies can provide first-hand results, detailed measurements are always difficult especially when information on flow quantities over a broad-range of time scale is needed.

In terms of the underlying physical mechanism, solubility trapping in a porous medium is analogous to the thermal convection with insulated boundaries in some respects [11]. Similar to the thermal boundary layer in thermal convection, a diffusive boundary layer in solubility trapping can be defined, which becomes unstable only after an initial incubation period of the small perturbation [6]. After this initial period, convection can be triggered. Rayleigh number is an important parameter to describe the stability of such a system in porous media [24], which compares the convective rate with the diffusive rate. It can be defined as [6]:

$$Ra = \frac{K\Delta\rho gH}{\phi D\mu} \quad (1)$$

If the rate of fluid convection exceeds the rate at which the density increase is diffusively redistributed, convection will occur [16]. Theoretical analyses [26,27] have indicated that the convection is expected only if  $Ra > 4\pi^2$ .

Numerical studies may fill the gaps of theoretical and experimental studies. On one hand, numerical results can verify the linear stability analysis; on the other hand, they can provide more

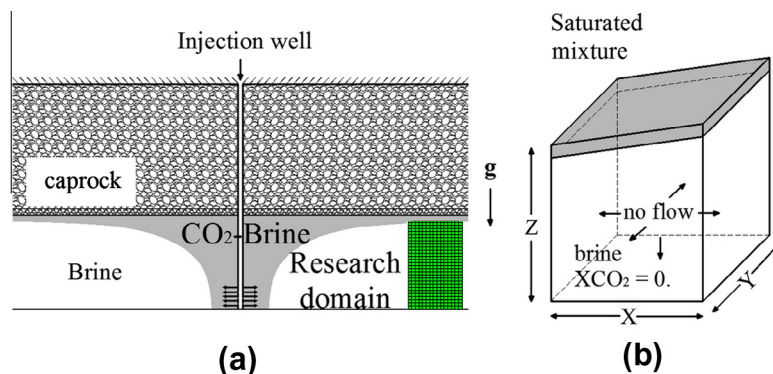


Fig. 1. Schematic representation of CO<sub>2</sub> solubility trapping in geological storage formation (a) and computational domains (b).

detailed information to highlight the physical mechanisms of convection instability. In numerical studies, it is possible to investigate both the short-term and long-term behaviours of solubility trapping process, but assumptions are always employed to simplify the problem. In many studies [6,22–24,28,29], the incompressibility and Boussinesq assumption were employed, while the full compressible model was less commonly used [3]. In order to reduce the computational costs, most of the numerical simulations were carried out in 2D. Simulations carried out in 2D have limitations as shown by Pau et al. [7]. In addition, the caprocks in certain targeted CO<sub>2</sub> geological storage formations may have slopes, which will affect the flow of gas and aqueous phase [30–34] but have not been investigated in detail. In this case, the gravitational force is no longer normal to the caprock surface, which can further enhance the multi-dimensional nature of the process. It remains unclear what kind of role 3D effects may play in the fluid dynamic behaviours of solubility trapping.

In this study, numerical simulations are used to investigate the physical process of solubility trapping to obtain a better understanding of the 3D effects on solubility trapping including the effects of inclined caprock surface. The paper is organised as follows. In Section 2, the governing equations, the numerical methods and resolutions, and the initial and boundary conditions used in the simulations are given. In Section 3, the fluid dynamic behaviours of density driven fingering under different conditions including the effects of inclined caprock surfaces are examined. Finally, conclusions from the study are drawn.

## 2. Problem and methods

Most studies were carried out with horizontal caprocks considered in the physical model, but some geological formations possess naturally inclined caprock. Important examples include the Carrizo-Wicox aquifer and the Mt. Simon aquifer in the US, and saline aquifer in the Alberta Basin in Canada [30–32]. In this case, the CO<sub>2</sub> plume would preferentially migrate along the inclination due to the buoyancy. For the solubility trapping, the flow behaviours of aqueous phase in the inclined cases are different from that of the horizontal cases. The gravitational force is no longer normal to the caprock surface; hence, density-driven fingering caused by the gravitational instability may present more complicated features. Motivated by naturally inclined geological formations, comparisons of the dissolving process and instantaneous behaviours between the two cases are needed.

After injection, CO<sub>2</sub> will likely locate under the caprock and there will be an interface formed between the free CO<sub>2</sub>-rich phase above and the brine phase below, as shown in Fig. 1(a). For simplicity, the interface can be assumed to be flat as shown in Fig. 1(b). Two scenarios are considered in this study in terms of the orientation of the caprock surface: normal to the gravity and inclined with an angle. In the case of inclined caprock, since pressure increases with the depth in the subsurface and the dissolved CO<sub>2</sub> mass fraction in brine increases with pressure [2], the dissolved CO<sub>2</sub> concentration is affected by the inclination of caprock. However, the physical domain sizes and the inclinations are small in this study, so the variations of concentration of dissolved CO<sub>2</sub> along the caprock are omitted. At the interface, the dissolved CO<sub>2</sub> will be transported downward by molecular diffusion in the aqueous phase, which is very slow unless the convection occurs. To avoid dealing with complicated capillary force of two-phase flow, the top boundary is modelled by a condition of constant saturated concentration of dissolved CO<sub>2</sub> in brine [9].

Since 3D simulations are significantly more resources-intensive, most of the analyses for this problem were based on 2D models. Although some important relations, for instance, the

relations between the onset time of convection, critical wavelength and critical depth of diffusive layer and Rayleigh number, were obtained using 2D simulations, 2D simulations still have some limitations, such as the fingering structures and the flow behaviours. 3D simulations add a degree of freedom to the fingering phenomena and thus increase the complexity. Comparisons between 2D and 3D simulations of the diffusion-convection process are needed to determine whether the 3D results will be significantly different from 2D simulations. Both 2D and 3D cases are considered in this study. Moreover, geochemical reactions which generally occur at long time scales [35] are neglected in this case. Accordingly CO<sub>2</sub> acts as a conservative solute tracer in the computational domain [3].

### 2.1. Governing equations

The integral form of mass conservation equation is used, which is given by [1,36]:

$$\frac{\partial}{\partial t} \int_{V_n} \phi \rho X_i dV_n + \int_{V_n} \nabla \cdot (\rho X_i \mathbf{q}) dV_n = \int_{V_n} \nabla \cdot (\phi D \rho \nabla X_i) dV_n \quad (2)$$

By using Gauss theorem, the integration of Eq. (2) in each control volume or mesh can be written as:

$$\frac{\partial}{\partial t} \int_{V_n} \phi \rho X_i dV_n = \int_{S_n} (\rho X_i \mathbf{q}) \cdot \mathbf{n} dS_n - \int_{S_n} (\phi D \rho \nabla X_i) \cdot \mathbf{n} dS_n \quad (3)$$

where  $\mathbf{n}$  is the normal vector on the surface element  $dS_n$  (assumed pointing inward into the mesh  $n$ ).

The description for the flow of a fluid through a porous media can be given by Darcy's law. It can be described in a vector form as [37]:

$$\mathbf{q} = -\frac{K}{\mu} (\nabla P - \rho \mathbf{g}) \quad (4)$$

where  $\mathbf{q}$  is a vector quantity representing discharge per unit area. Darcy's law is an approximate form of the fluid momentum balance in creeping flow through porous media. The law is only valid for steady, slow viscous flow, which can be derived from the Navier–Stokes momentum equations.

The dynamic viscosity of aqueous phase in Eq. (4) is assumed to be the same as the pure brine, with the assumption that the effect of dissolved CO<sub>2</sub> can be neglected [38].

Eq. (2) is constructed by three terms representing the time rate of change of mass at a fixed location, convective and diffusive transports, respectively [1]. In this application, thermal effects and temperature changes are neglected so that the energy conservation equation can be omitted, i.e., an isothermal condition is considered.

For the system studied here, two primary variables are necessary to identify the thermodynamic state, which are the pressure,  $P$ , and the dissolved CO<sub>2</sub> mass fraction,  $X_2$ . Three secondary variables are velocity vector,  $\mathbf{q}$ , brine mass fraction,  $X_1$ , and aqueous density,  $\rho$ , which are needed to assemble the mass conservation equations. There are three equations for the five variables; therefore, to close the system equations an additional two independent relations are required. The problem is closed by the following relations.

Mass fractions sum to unity:

$$X_1 + X_2 = 1 \quad (5)$$

The density of aqueous mixture with dissolved CO<sub>2</sub> is calculated from [7]:

$$\frac{1}{\rho} = \frac{X_1}{\rho_1} + \frac{X_2}{\rho_2} \quad (6)$$

where the partial density of pure brine and the dissolved CO<sub>2</sub> mass fraction are both functions of temperature, pressure and salt mass fraction, calculated by Battistelli et al. [38] and Spycher and Pruess [5], respectively.

The partial density of dissolved CO<sub>2</sub> in Eq. (6) is calculated from:

$$\rho_2 = \frac{M_{\text{CO}_2}}{V_\phi} \quad (7)$$

where  $V_\phi$  is a function of temperature and independent of pressure, given by García [39]. In this work,  $T$  is a constant, accordingly  $V_\phi = 34.92 \times 10^{-6} \text{ m}^3/\text{mol}$  is used.  $M_{\text{CO}_2}$  is equal to  $44.0 \times 10^{-3} \text{ kg/mol}$ . When the two values are substituted into Eq. (7),  $\rho_2 = 1260 \text{ kg/m}^3$  is obtained. In the above, Eq. (6) shows that the density of aqueous mixture increases when CO<sub>2</sub> dissolves into the brine at the reservoir conditions.

Eqs. (2)–(7) constitute the fundamental governing equations for numerical simulations of the flow in porous media for solubility trapping, which are a set of coupled nonlinear equations and could be solved by Newton–Raphson iteration.

## 2.2. Numerical method

Eqs. (2) and (3) are discretized in time using an implicit finite difference scheme and in space using an integral finite difference method. The discretization method, the spatial and temporal resolutions used in the simulations are described as follows.

For the discretization, the accumulation terms are discretized by introducing appropriate volume averages:

$$\frac{\partial}{\partial t} \int_{V_n} \phi \rho X_i dV_n = \left( \phi_n^{t+\Delta t} \rho_n^{t+\Delta t} X_{i,n}^{t+\Delta t} - \phi_n^t \rho_n^t X_{i,n}^t \right) \cdot \frac{V_n}{\Delta t} \quad (8)$$

where  $t + \Delta t$  represents the new time step.

The fluxes of convective and diffusive terms are approximated as a discrete sum of averages over all surfaces of meshes,

$$\int_{S_n} (\rho X_i \mathbf{q}) \cdot \mathbf{n} dS_n = \sum_m \rho_{nm}^{t+\Delta t} X_{i,nm}^{t+\Delta t} q_{nm}^{t+\Delta t} S_{nm} \quad (9)$$

$$\int_{S_n} (\phi D \rho \nabla X_i) \cdot \mathbf{n} dS_n = \sum_m \phi D \rho_{nm}^{t+\Delta t} \nabla X_{i,nm}^{t+\Delta t} S_{nm} \quad (10)$$

where these flux terms are treated as fully implicit, given by the values at the new time step.

The Darcy's law is discretized in the following way [40],

$$q_{nm}^{t+\Delta t} = - \left( \frac{K}{\mu} \right)_{nm} \left( \frac{p_n^{t+\Delta t} - p_m^{t+\Delta t}}{D_{nm}} + \rho_{nm}^{t+\Delta t} g \cos \alpha \right) \quad (11)$$

where  $\alpha$  is the intersection angle between gravitational acceleration and the line segment from mesh  $m$  to  $n$  with rotation direction from  $\mathbf{g}$  to the line segment clockwise as indicated in Fig. 2.

In Eq. (11),  $\cos \alpha$  can be written as follows:

$$\cos \alpha = \frac{Z_2 - Z_1}{D_{nm}} \quad (12)$$

where  $Z_1, Z_2$  are the respective grid block elevations. The Darcy's law between mesh  $m$  and  $n$  is then written as

$$q_{nm}^{t+\Delta t} = - \left( \frac{K}{\mu} \right)_{nm} \left( \frac{p_n^{t+\Delta t} - p_m^{t+\Delta t}}{D_{nm}} + \rho_{nm}^{t+\Delta t} g \frac{Z_2 - Z_1}{D_{nm}} \right) \quad (13)$$

where  $\rho_{nm}, X_{i,nm}, (K/\mu)_{nm}$  are the harmonic averages between meshes  $m$  and  $n$ , given by,

$$\rho_{nm} = \frac{D_1 \rho_m + D_2 \rho_n}{D_{nm}} \quad (14)$$

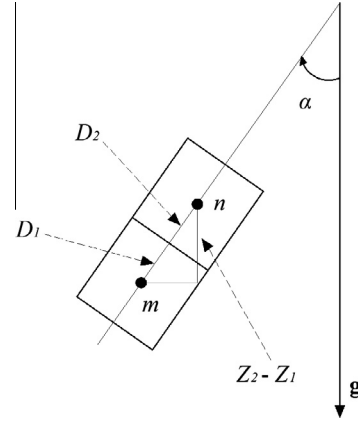


Fig. 2. Spatial discretization considered in this study.

$$X_{i,nm} = \frac{D_1 X_{i,m} + D_2 X_{i,n}}{D_{nm}} \quad (15)$$

$$\left( \frac{K}{\mu} \right)_{nm} = \frac{D_1 (K/\mu)_m + D_2 (K/\mu)_n}{D_{nm}} \quad (16)$$

where  $D_{nm}$  is given as:

$$D_{nm} = D_1 + D_2 \quad (17)$$

## 2.3. The consideration of resolutions

Evolution and interaction of flow and transport over a broad range of space and time scales are essential features of the solubility trapping. Therefore temporal and spatial resolutions have to be adequate to resolve the essential flow features. In order to capture the early stage diffusive behaviours and obtain the onset time of convection accurately, a small time step of 0.01 s is used. At the same time, due to the long-term behaviours of this problem, an automatic time step adjustment scheme is used to track the process accurately and effectively, by changing the time steps according to the variations of solutions between adjacent time steps.

The spatial resolution should be able to resolve the concentration gradients that drive the process. The diffusive boundary layer depends on the formation and fluid properties, where the gradients can be rather large, not only because the thickness of diffusive boundary layer is quite thin, but also because some regions near the top boundary layer are compressed due to the upwelling water with low CO<sub>2</sub> concentration after the onset of convection. For the vertical discretization, the grid block sizes near the top boundary are chosen such that they are sufficiently smaller than the thickness of the diffusive boundary layer obtained by linear stability analysis, while a larger grid resolution is used in other regions. The penetration depth at the onset of instability is given as  $\delta_c = 34 \mu \phi D / (K \Delta \rho g) = 12 \text{ mm}$  [3]. A vertical grid is set to be 1 mm near the top boundary, which is able to resolve the gradients of dissolved CO<sub>2</sub> concentrations. Away from the top boundary, vertical grid spacing was stretched from 1 mm to 1 cm. Horizontal grid resolution is set up to be smaller than the size of the critical wavelength. The critical wavelength is given as  $\lambda_c = 96.23 \mu \phi D / (K \Delta \rho g) = 34 \text{ mm}$  [14]. A horizontal grid resolution of 1 cm is used to capture the convective transport and the resulting solubility trapping.

In order to obtain a better understanding on how the grid resolution affects the numerical solutions, grid dependence is examined for the 2D simulations with the physical domain size of  $1 \text{ m} \times 1 \text{ m}$ . According to the discretization method discussed above, the model is partitioned into  $100 \times 134$  points. The domain

is meshed with rectangles, and the number of elements is increased from  $25 \times 34$  to  $200 \times 268$  with total dissolved  $\text{CO}_2$  (i.e. inventory) results shown in Fig. 3(a). It is evident that the mesh with  $100 \times 134$  points is sufficient to solve this problem.

#### 2.4. Initial and boundary conditions

In real reservoir systems, unstable fluid flow is usually triggered by geologic heterogeneity and/or fluid heterogeneity [25]. The perturbation is introduced by an isotropic permeability with small random disturbances [3]. The porosity and diffusivity are identical in the entire field. In order to suppress the convection of  $\text{CO}_2$ -rich brine from the top boundary and ensure that the mass transport across the upper boundary is only by molecular diffusion, the top boundary condition is given by specifying a very small permeability. The other boundary conditions are set to be no flux, i.e., there is no fluid flow across these boundaries at all times, shown in Fig. 1(b). Fig. 3(b) shows  $\text{CO}_2$  dissolving rates for different salt concentration, illustrating decreasing flux and increasing onset time of convection. The effect can be explained by the decreasing concentration of dissolved  $\text{CO}_2$  with the increase of salt mass fraction in brine [41]. In order to capture the dynamic behaviours quickly and effectively, there are no salt in brine in the following cases. The initial conditions, fluid and formation properties, as specified in Table 1, are typical underground supercritical conditions at 1000 m depth. For the purpose of capturing the dynamic behaviours of solubility and understanding the growth mechanism of the fingers, several 2D and 3D test cases are performed. The domain sizes, inclined angles and Rayleigh numbers are in Table 2.

### 3. Results and discussion

The evolution of solubility trapping follows the transition from a diffusion-dominated flow to a convection-dominated flow [7]. During the diffusion-dominated period, the diffusion provides driving force to thicken the diffusive boundary layer and to trigger the convection under appropriate conditions. While during the convective-dominated periods, the convection leads to nonlinear behaviours and promotes  $\text{CO}_2$  near the top boundary dissolving into the aqueous phase underneath. Both 2D and 3D simulations are carried out and the differences between these simulations are compared.

#### 3.1. 2D simulation results

In this case, the long-term behaviours of evolution and interaction of  $\text{CO}_2$  plumes at three different Rayleigh numbers, i.e.,

**Table 1**  
Initial conditions, fluid and formation properties.

<i>Initial conditions</i>	
Temperature	$T = 45^\circ\text{C}$
Pressure	$P = 100$ bars
Salinity	$X_s = 0$
Dissolved $\text{CO}_2$ concentration	$X_1 = 0$
<i>Fluid properties</i>	
Pure water density	$994.56 \text{ kg/m}^3$
Saturated $\text{CO}_2$ mass fraction	$0.049306$ [35]
Diffusivity	$D = 2 \times 10^{-9} \text{ m}^2/\text{s}$
<i>Formation properties</i>	
Porosity	$\phi = 0.3$
Permeability	$K = 10^{-11} \text{ m}^2$

**Table 2**  
Model sizes, inclined angles and Rayleigh numbers.

Cases	X (m)	Y (m)	Z (m)	Angles	Ra
2D	1.0	–	1.0	$0^\circ$	862
	1.0	–	2.5	$0^\circ$	2155
	1.0	–	5.0	$0^\circ$	4310
	1.0	–	1.0	$5^\circ$	862
	1.0	–	1.0	$10^\circ$	862
	1.0	–	1.0	$20^\circ$	862
3D	1.0	1.0	1.0	$0^\circ$	862
	1.0	1.0	2.5	$0^\circ$	862
	1.0	1.0	1.0	$5^\circ$	862
	1.0	1.0	1.0	$10^\circ$	862

different thicknesses of simulation zone, have been studied. The results are shown in terms of contour maps of  $\text{CO}_2$  concentration and  $\text{CO}_2$  dissolving fluxes at the top boundary.

Fig. 4 shows the dissolved  $\text{CO}_2$  contour maps at different stages for  $Ra = 862$ , illustrating the evolution of solubility trapping. Fig. 4(a) corresponds to a moment immediately after the onset of convection. The diffusive boundary layer transported downward has been distorted at the top boundary. The denser fluid is transported downward while the lighter aqueous phase flows upward due to the convection. In this stage, some regions in diffusive boundary layer are compressed. In the meantime, increasingly enhanced horizontal flow could trigger the development of nonlinear dynamics such as coalescing and merging, so the convective fingers become broader at subsequent time instants, as shown in Fig. 4(b). The driving force of nonlinear dynamics is the concentration gradient. This process continues as time progresses. Fig. 4(c) corresponds to the period that convection speed tends to be steady.

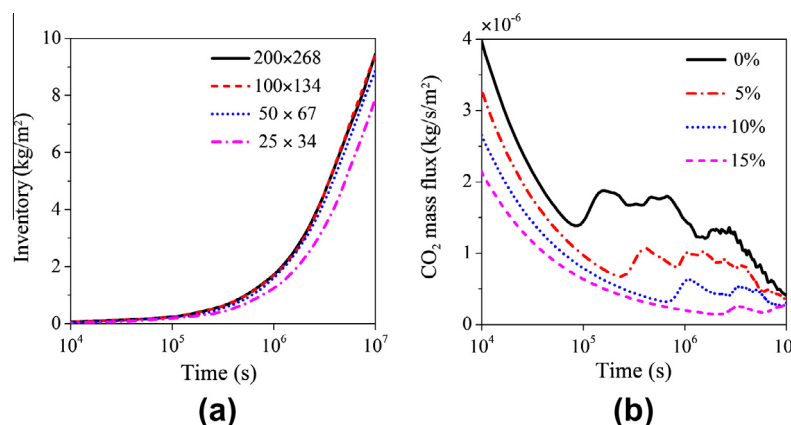


**Fig. 3.** Inventory at different resolutions (a), and  $\text{CO}_2$  dissolving rates with different salt concentrations (b).



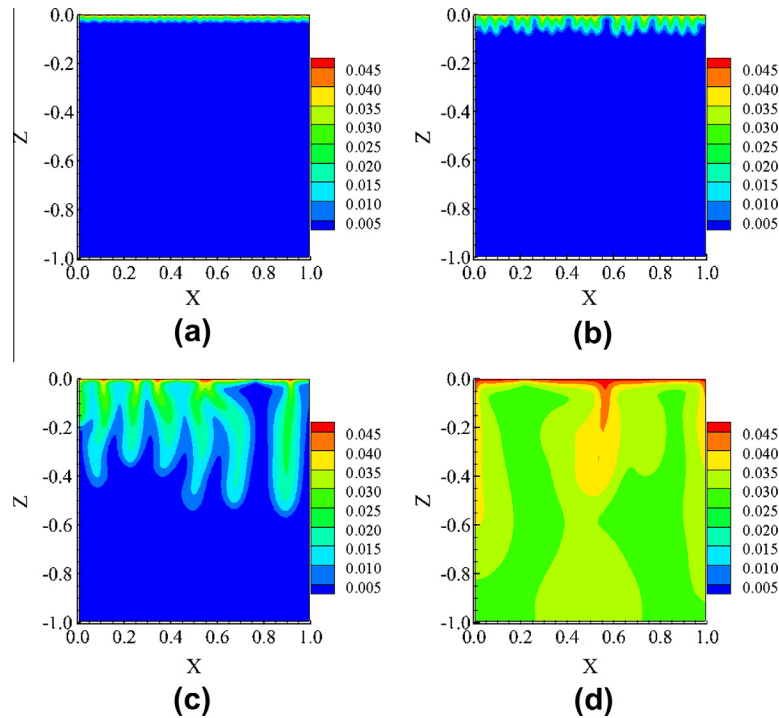


Fig. 4. Simulated distribution of 2D dissolved CO<sub>2</sub> at different time instants: (a)  $t = 1.e5$  s, (b)  $t = 2.e5$  s, (c)  $t = 1.e6$  s and (d)  $t = 1.e7$  s.

The fingers advance downward unceasingly and the fingers become fewer. Some larger fingers travel more or less independently with less interaction with their neighbouring fingers. These fingers undergo strong nonlinear dynamics such as shift in the feeding sites and lateral pinch-off. Fig. 4(d) corresponds to the stage when the convection has been decayed. The fingers have reached the bottom of the zone. Once the fingers touch the bottom boundary, the aquifer boundary will affect the mixing process and the interactions between fingers become less important than the bottom boundary effect. The dissolved CO<sub>2</sub> contour maps shown in Fig. 4 indicate strong nonlinear behaviours, which become more evident in the evolution of CO<sub>2</sub> dissolving rates shown in Fig. 5.

Fig. 5(a) illustrates the CO<sub>2</sub> mass fluxes at the top boundary for different Rayleigh numbers together with analytical mass flux at the top boundary considering pure diffusion only, which have been plotted in logarithmic scale. The rate of CO<sub>2</sub> uptake at the dissolution boundary ( $Z = 0$ ), per unit cross-sectional area, can be given as [3]:

$$F(Z = 0, t) = \phi \rho X_0 \sqrt{\frac{D}{\pi t}} \quad (18)$$

Eq. (16) illustrates analytically that diffusive mass flux without convection is inversely proportional to  $t^{0.5}$ , indicating that dissolution rate declines with time. However, the relation is changed to be non-monotonic since the onset of convection and the flux with convection is increased to several orders higher than the pure diffusive flux as shown in Fig. 5(a). The temporal evolution of CO<sub>2</sub> dissolution rate roughly follows four periods in time: diffusive period, modulated convective period, constant convective period and decay convective period, as shown by the dashed vertical lines for  $Ra = 4310$  in Fig. 5(b). In the diffusion dominated period (Period 1), the agreement between numerical results and analytical diffusive flux is good since diffusion is the only physical process for the three different Rayleigh numbers in this period. With the onset of convection, a general increase in dissolution rate is shown in the modulated convective period (Period 2). The partial coalescing and

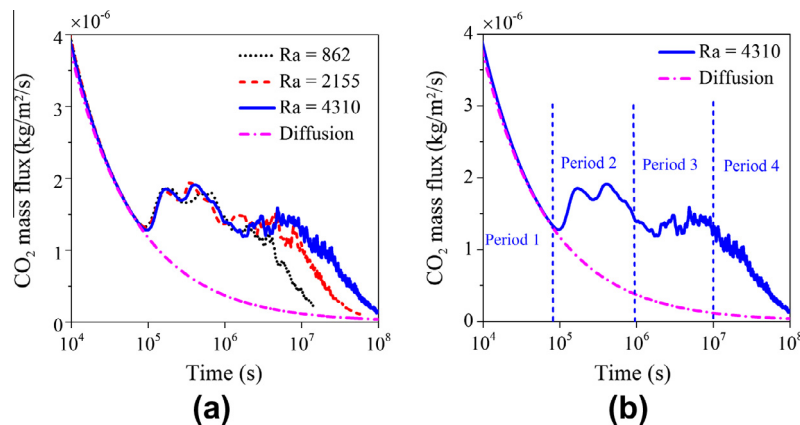


Fig. 5. 2D CO<sub>2</sub> dissolving rates compared with analytical results (pure diffusion) on logarithmic time scales (a), and the different periods in the evolution of the solubility trapping for  $Ra = 4310$  marked by the blue dashed vertical lines (b). (For interpretation of the references to colour in this figure legend, the reader is referred to the web version of this article.)

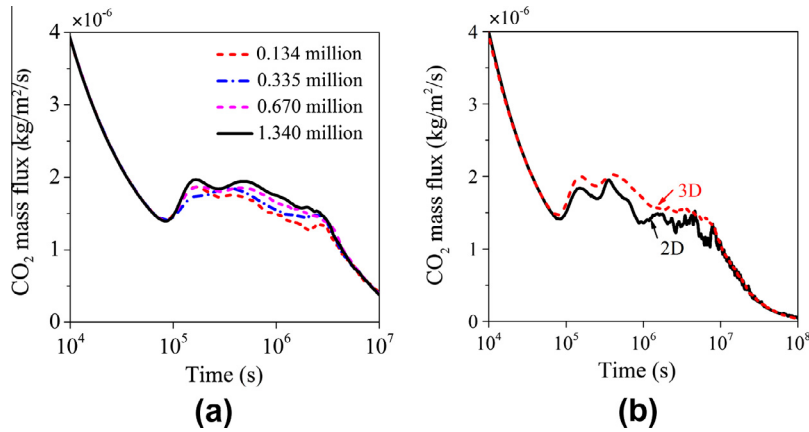


Fig. 6. Comparison of 3D CO<sub>2</sub> dissolving rates for different resolutions (a), and comparison of the results from 2D and 3D cases for  $Ra = 2155$ .

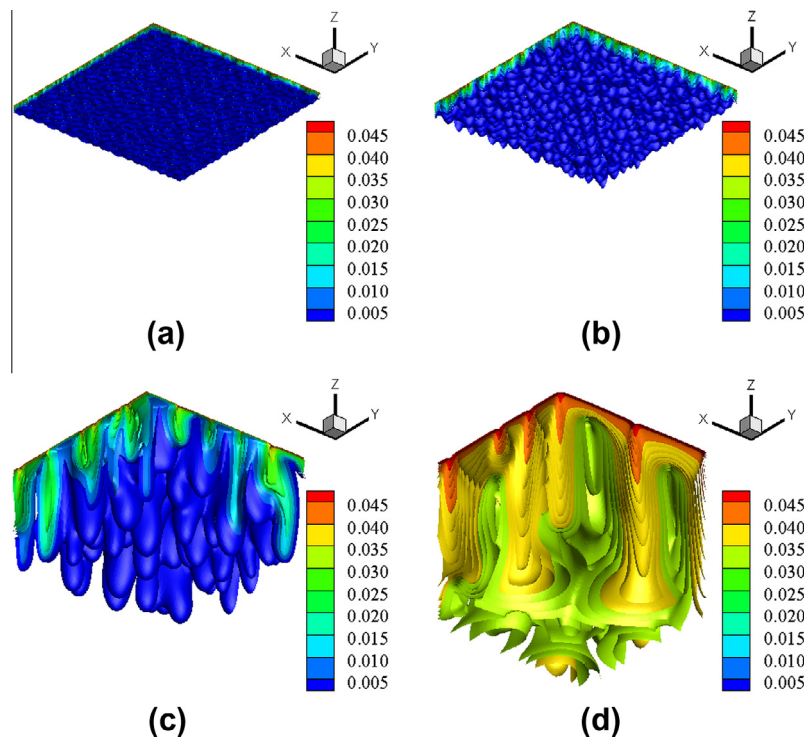


Fig. 7. Simulated distribution of dissolved CO<sub>2</sub> in 3D at different time instants: (a)  $t = 1.e5$  s, (b)  $t = 2.e5$  s, (c)  $t = 1.e6$  s and (d)  $t = 1.e7$  s.

growing of convective fingers result in an increase in the dissolution rates, where variations are observed at different Rayleigh numbers. In the third period, significant differences between the three Rayleigh numbers can be observed, and the duration is related to the thickness of formations. At the fourth period, the onset time of decayed convection increases with the Rayleigh number. However, it is observed that the slopes of the decay convective periods are approximately the same at different Rayleigh numbers. During the last stage of convection, the nonlinear dynamics gradually weakens, leading to a declining CO<sub>2</sub> dissolving rate. In Fig. 5(a) and (b), it can be seen that the dissolution process is dominated by the convection time, while the time taken for diffusion is much shorter.

### 3.2. 3D simulation results

In order to examine the 3D effects on solubility trapping, 3D simulations with different spatial resolutions were carried out

and compared with the 2D simulation. Due to the high demand of computational resources, the small and medium Rayleigh number cases ( $Ra = 862$  and  $Ra = 2155$ ) were examined. The 3D model used the same initial and boundary conditions, the fluid and formation parameters and grid resolution as the 2D cases. Four different spatial resolutions in Y axis are performed. The grid resolutions of these four cases in X axis and Z axis are the same, corresponding to the total numbers of meshes of 0.134, 0.335, 0.67 and 1.34 million, respectively.

Similar to the 2D cases, the evolution of CO<sub>2</sub> mass flux in the 3D simulations also exhibits four periods. However, the difference between the 2D and 3D results with different grid resolutions are obvious in terms of the evolution of dissolving rates as shown in Fig. 6(b). Since diffusion is initially dominating and uniform in all directions, the fluxes agree well at the early stage for all the 2D and 3D cases. However, the fluxes begin to be different since the onset of convection. Similar results are obtained with different resolutions in the Y-axis direction, as shown in Fig. 6(a). The stronger

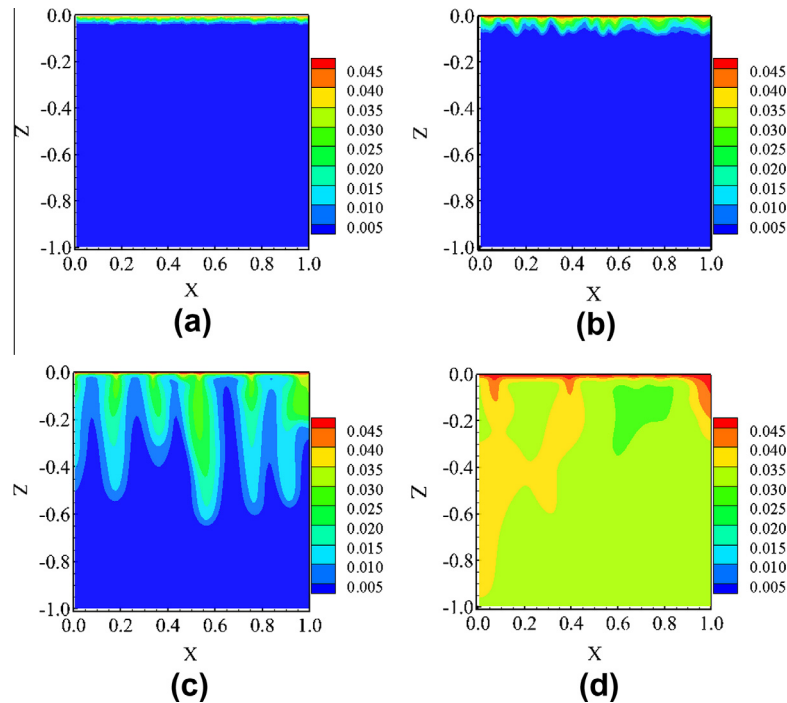


**Fig. 8.** Cross-sectional CO<sub>2</sub> contour maps in the mid-XZ plane of the 3D case at different time instants: (a)  $t = 1.e5$  s, (b)  $t = 2.e5$  s, (c)  $t = 1.e6$  s and (d)  $t = 1.e7$  s.

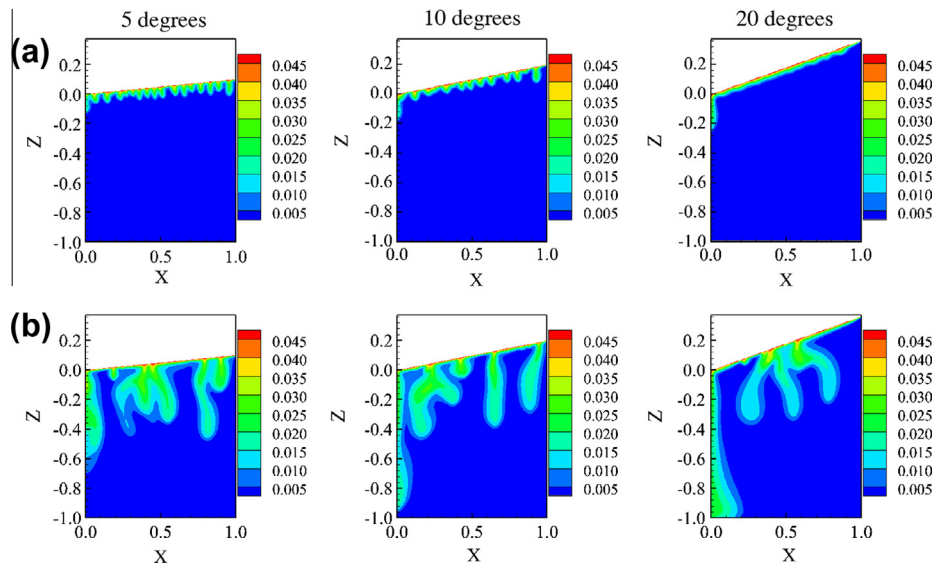


**Fig. 9.** Distribution of the dissolved CO<sub>2</sub> at different time instants: (a)  $t = 2.e5$  s and (b)  $t = 1.e6$  s for 5°, 10° and 20° of the 2D inclined cases.

dissolution and smaller fluctuation of the 3D results can be associated with the fact that the nonlinear dynamics is better predicted by the 3D simulation.

Fig. 7 shows the 3D dissolved CO<sub>2</sub> contour maps from the simulation using 1.34 million meshes, the time instants are the same as those of the 2D simulation as shown in Fig. 4. Fig. 7(a) corresponds to the onset of convection, indicating the 3D topology of CO<sub>2</sub> concentration which is missing in the 2D case. In the 3D simulation, the iso-surface of CO<sub>2</sub> concentration has developed into many ripples. As time progresses, the fingers have been transported downward, leading to the formation of large-scale structures, as shown in Fig. 7(b). A lot of fingers are competing with their respective neighbours. In Fig. 7(c), the fingers are transported

further downward. The merging of fingers can be seen in all directions due to laterally flow that is present in the whole section. The location of the finger front is farther than the 2D result, indicating that total inventory can be larger than that of the 2D case. Eventually, the leading edges of fingers have reached the bottom boundary as shown in Fig. 7(d).

In order to further illustrate the differences between the 2D and 3D simulation results, the cross-sectional contour plots of the 3D results are compared with the corresponding 2D results. Fig. 8 shows the contour maps in the middle cross-section of the 3D domain. There are obvious differences between Figs. 8 and 4. The diffusive boundary layer in Fig. 8(a) is thicker than that in Fig. 4(a) and the number of fingers is fewer compared with the



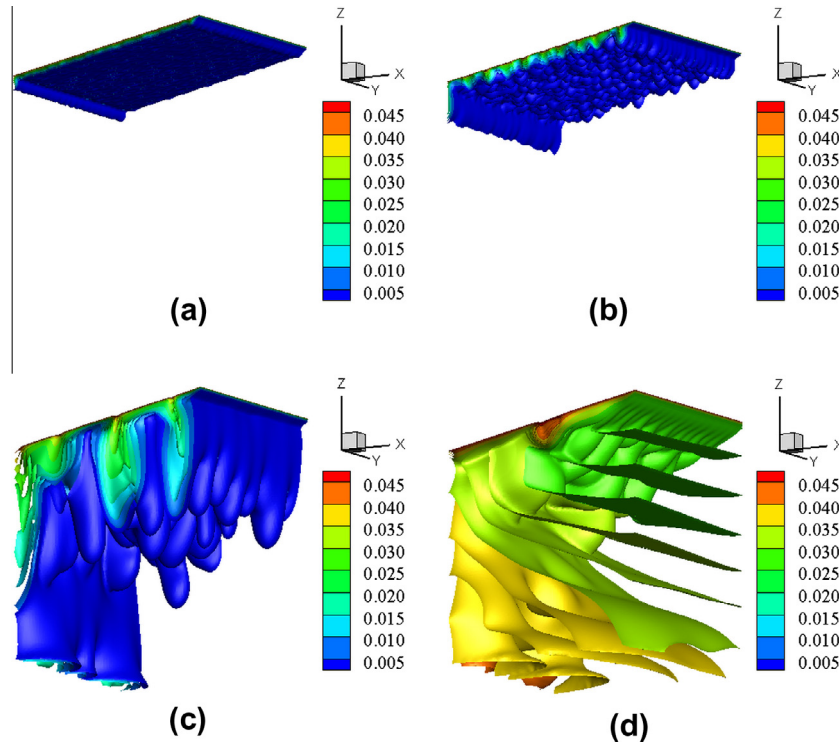


Fig. 10. Simulated distribution of dissolved CO<sub>2</sub> for the 3D 10° inclined case at different time instants: (a)  $t = 1.e5$  s, (b)  $t = 2.e5$  s, (c)  $t = 1.e6$  s and (d)  $t = 1.e7$  s.

2D result. In Fig. 8(b), the driving force for forming the large-scale fingers by nonlinear dynamics seems stronger than that in the 2D simulation, accordingly more CO<sub>2</sub> mass will be transported downward. In Fig. 8(c), the location of the deepest finger is farther than the results in Fig. 4(c). Hence, the fingers will be transported faster with more CO<sub>2</sub> moving downward. In Fig. 8(d), the total area of relatively high concentration is larger than the 2D result, which indicates that the total inventory is greater than the 2D result.

### 3.3. Simulations with inclined caprock surfaces

The long-term evolution of solubility trapping in a saline aquifer with inclined caprock surfaces by 2D simulations is considered,

as shown in Fig. 9. Compared with the 2D simulation with a horizontal caprock surface shown in Fig. 4, there are some differences, mainly in the diffusive boundary layer thickness, the position, the number and the dynamic changes of the fingers. It is observed that the diffusive boundary layer becomes smoother with the increase of the inclined angle, indicating that the flow is becoming more stable with increasing angle. As the angle increases, the number of fingers generally decreases. Hence, the nonlinear dynamics such as coalescing and merging of fingers develop very differently in comparison with the cases with a horizontal caprock surface.

In order to examine the 3D effects of inclined angles on the solubility trapping, 3D simulations with inclined caprock surfaces were carried out. Fig. 10 shows the 3D dissolved CO<sub>2</sub> contour maps

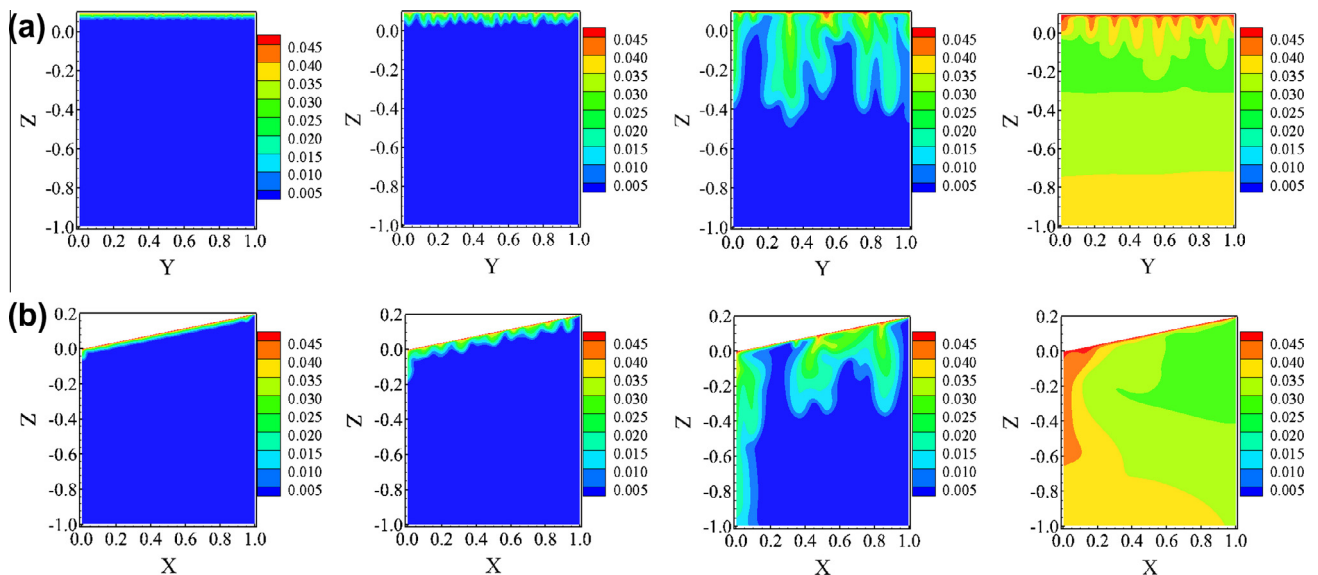


Fig. 11. Cross-sectional CO<sub>2</sub> contour maps in the mid-XZ plane (a) and mid-YZ plane (b) at different time instants ( $1.e5$  s,  $2.e5$  s,  $1.e6$  s and  $1.e7$  s) for the 3D 10° inclined case.

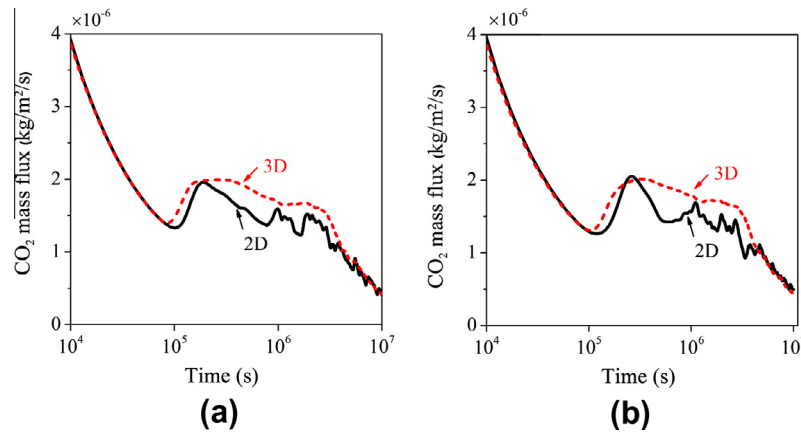


Fig. 12. Comparison of CO<sub>2</sub> mass fluxes at the top boundary for the 5° inclined cases (a) and the 10° inclined cases (b) from the 2D and 3D simulations.

with an inclined angle of 10°. Unlike the normal case shown in Fig. 7, the number of fingers is reduced and the fingering phenomenon becomes less obvious. The colliding and merging of fingers are weakened. It is evident that the flow affected by the gravity influences the generation and interaction of fingers in this inclined case. Fig. 11 shows the cross-sectional contour maps in the mid-XZ plane (a) and mid-YZ plane (b) at different time instants for the 3D case. The contour maps in the two planes are distinctively different. When the fingers on the far left side reach the bottom boundary, the fingers of other positions will be affected.

Fig. 12(a) and (b) illustrate the evolution of the CO<sub>2</sub> mass fluxes at the top boundary for the 2D and 3D cases with inclined angles. Agreement among all the cases is good in the diffusion stage, indicating that there is little impact of different angles on the diffusion. Unlike the behaviours of the diffusion period, the fluxes in the convective period for inclined cases show delayed onset time of convection compared with the flux for the normal case, all of which indicate that the interaction and interplay of fingers are attenuated. The later onset time of convection for the inclined cases is because that the gravity component perpendicular to the caprock is smaller and the component parallel to the caprock is larger with increased angle, which will make the boundary layer at the top boundary more difficult to satisfy the needed thickness for the development of the flow instability. Owing to the enhanced interaction of fingers, the flux curves for the 3D inclined cases show earlier onset time of convection and smoother variation during the convective period than the 2D inclined cases. All of these suggest that the trends of the fluxes in the 2D and 3D inclined cases are different, while the 2D results cannot be used for the prediction of solubility trapping in cases where the caprock has slopes.

#### 4. Conclusions

Both 2D and 3D numerical simulations of solubility trapping are performed to study the physical process of “viscous fingering” and differences between the 2D and 3D simulations are examined. Some insights have been obtained into the physics of density driven fingering including the three-dimensional effects on solubility trapping.

For the 2D normal cases, three reservoirs with the same properties and different thicknesses are studied. The results indicate that there are four distinctive time periods in the temporal evolution of CO<sub>2</sub> dissolution process. The onset time is independent of the thickness of reservoirs indicating that the thicknesses of diffusive boundary layer are much less than the thicknesses of reservoirs.

The duration of constant speed convection and the onset time of decayed convection directly depend on the Rayleigh number.

For the 3D normal cases, different grid resolutions with the same properties are studied. The results indicate that 2D simulations can approximate 3D simulations with low spatial resolution in the third spatial direction. In all the 3D cases, the fluxes agree well with the 2D results at the early stages of the fingering process mainly because the diffusion is initially dominating and uniform in all directions. However, the 3D flux is larger while the fluctuation of the 3D flux is smaller compared with the 2D case since the onset of convection. The increase of grid resolution leads to the prediction of smoother finger tips. The analyses show that the 3D effects could be important in the constant convective period and the subsequent stages of flow development while they might be neglected in predicting the onset of convection.

For the 2D and 3D inclined cases, different behaviours are observed during the fingering process. The evolution of dissolving flux is also different compared with the normal cases. The number of fingers is reduced and the interaction of fingers is weakened with the increase of the inclined angle. The fluxes of the 3D inclined cases show later onset time of convection than the 3D normal case and earlier onset than the 2D inclined cases. The results of the inclined cases show a clear directional dependence. Moreover, the simulations indicate that the 2D results cannot be used for the prediction of the solubility trapping in the inclined cases.

In summary, the numerical analyses highlight the physical mechanisms of solubility trapping. However, several assumptions were introduced to simplify this problem, such as the homogeneity of porous medium, single phase flow and no geochemical reaction, which are expected to play an important role in real development of fingering. Moreover, the physical problem needs very fine mesh to resolve the concentration near the interface, accordingly a prohibitive amount of computing resources would be required in large-scale simulations for practical applications. In order to effectively capture the behaviours of fingering in full-scale carbon storage, sub-grid scale dynamics may be modelled in an upscaling approach of the physical problem on a given time scale, which is being carried out.

#### Acknowledgements

This work was supported by the Thousand Talent Program of China, China Postdoctoral Foundation (Project No. 2012M521253), National Natural Science Foundation of China (No. 51106147), National Basic Research Program of China (973 Program: No. 2012CB719701) and Fundamental Research Funds for the Central

Universities (Nos. WK2320000006 and WK2320000025). The authors thankfully acknowledge all these supports.

## References

- [1] Jiang X. A review of physical modelling and numerical simulation of long-term geological storage of CO<sub>2</sub>. *Appl Energy* 2011;88(11):3557–66.
- [2] Bachu S. CO<sub>2</sub> storage in geological media: role, means, status and barriers to deployment. *Prog Energy Combust Sci* 2008;34(2):254–73.
- [3] Pruess K, Zhang K. Numerical modeling studies of the dissolution-diffusion-convection process during CO<sub>2</sub> storage in saline aquifers. Technical report LBNL-1243E. Lawrence Berkeley National Laboratory, California; 2008.
- [4] Pruess K, Spycher N. ECO2N – a fluid property module for the TOUGH2 code for studies of CO<sub>2</sub> storage in saline aquifers. *Energy Convers Manage* 2007;48(6):1761–7.
- [5] Spycher N, Pruess K. CO<sub>2</sub>–H<sub>2</sub>O mixtures in the geological sequestration of CO<sub>2</sub>. II. Partitioning in chloride brines at 12–100 °C and up to 600 bar. *Geochim Cosmochim Acta* 2005;69(13):3309–20.
- [6] Riaz A, Hesse M, Tchelepi HA, Orr FM. Onset of convection in a gravitationally unstable diffusive boundary layer in porous media. *J Fluid Mech* 2006;548:87–111.
- [7] Pau GSH, Bell JB, Pruess K, Almgren AS, Lijewski MJ, Zhang KN. High-resolution simulation and characterization of density-driven flow in CO<sub>2</sub> storage in saline aquifers. *Adv Water Resour* 2010;33(4):443–55.
- [8] Weir GJ, White SP, Kissling WM. Reservoir storage and containment of greenhouse gases. *Energy Convers Manage* 1995;36(6–9):531–4.
- [9] Ennis-King J, Paterson L. Rate of dissolution due to convective mixing in the underground storage of carbon dioxide. Amsterdam: Elsevier Science BV; 2003.
- [10] Ennis-King J, Paterson L. Role of convective mixing in the long-term storage of carbon dioxide in deep saline formations. *SPE J* 2005;10(3):349–56.
- [11] Lindeberg E, Wessel-Berg D. Vertical convection in an aquifer column under a gas cap of CO<sub>2</sub>. *Energy Convers Manage* 1997;38(Supplement):S229–34.
- [12] Ennis-King J, Preston I, Paterson L. Onset of convection in anisotropic porous media subject to a rapid change in boundary conditions. *Phys Fluids* 2005;17(8):1–15.
- [13] Hassanzadeh H, Pooladi-Darvish M, Keith DW. Stability of a fluid in a horizontal saturated porous layer: effect of non-linear concentration profile, initial, and boundary conditions. *Transp Porous Med* 2006;65(2):193–211.
- [14] Xu X, Chen S, Zhang D. Convective stability analysis of the long-term storage of carbon dioxide in deep saline aquifers. *Adv Water Resour* 2006;29(3):397–407.
- [15] Ennis-King J, Paterson L. Coupling of geochemical reactions and convective mixing in the long-term geological storage of carbon dioxide. *Int J Greenh Gas Control* 2007;1(1):86–93.
- [16] Kneafsey TJ, Pruess K. Laboratory experiments and numerical simulation studies of convectively enhanced carbon dioxide dissolution. *Energy Procedia* 2011;4:5114–21.
- [17] Kneafsey T, Pruess K. Laboratory flow experiments for visualizing carbon dioxide-induced, density-driven brine convection. *Transp Porous Med* 2010;82(1):123–39.
- [18] Yang C, Gu Y. Accelerated mass transfer of CO<sub>2</sub> in reservoir brine due to density-driven natural convection at high pressures and elevated temperatures. *Ind Eng Chem Res* 2005;45(8):2430–6.
- [19] Simmons CT, Pierini ML, Hutson JL. Laboratory investigation of variable-density flow and solute transport in unsaturated-saturated porous media. *Transp Porous Med* 2002;47(2):215–44.
- [20] Neufeld JA, Hesse MA, Riaz A, Hallworth MA, Tchelepi HA, Huppert HE. Convective dissolution of carbon dioxide in saline aquifers. *Geophys Res Lett* 2010;37(22):L22404. <http://dx.doi.org/10.1029/2010GL044728>.
- [21] Backhaus S, Turitsyn K, Ecke RE. Convective instability and mass transport of diffusion layers in a hele-shaw geometry. *Phys Rev Lett* 2011;106(10):104501. <http://dx.doi.org/10.1103/PhysRevLett.106.104501>.
- [22] Lindeberg E, Bergmo P. The long-term fate of CO<sub>2</sub> injected into an aquifer. Amsterdam: Elsevier Science BV; 2003.
- [23] Farajzadeh R, Salimi H, Zitha PLJ, Bruining H. Numerical simulation of density-driven natural convection in porous media with application for CO<sub>2</sub> injection projects. *Int J Heat Mass Transfer* 2007;50(25–26):5054–64.
- [24] Hassanzadeh H, Pooladi-Darvish M, Keith DW. Scaling behaviour of convective mixing, with application to geological storage of CO<sub>2</sub>. *AIChE J* 2007;53(5):1121–31.
- [25] Xie Y, Simmons CT, Werner AD. Speed of free convective fingering in porous media. *Water Resour Res* 2011;47(11):W11501. <http://dx.doi.org/10.1029/2011WR010555>.
- [26] Horton CW, Rogers FT. Convection currents in a porous medium. *J Appl Phys* 1945;16(6):367–70.
- [27] Wooding RA. Steady state free thermal convection of liquid in a saturated permeable medium. *J Fluid Mech* 1957;2(3):273–85.
- [28] Hesse M. Mathematical modeling and multiscale simulation of CO<sub>2</sub> storage in saline aquifers. PhD dissertation. Stanford University, Stanford, California; 2008.
- [29] Hassanzadeh H, Pooladi-Darvish M, Keith DW. Modelling of convective mixing in CO<sub>2</sub> storage. *J Can Pet Technol* 2005;44(10):43–51.
- [30] Nicot J-P. Evaluation of large-scale CO<sub>2</sub> storage on fresh-water sections of aquifers: an example from the Texas Gulf Coast Basin. *Int J Greenh Gas Con* 2008;2(4):582–93.
- [31] Birkholzer JT, Zhou Q, Tsang C-F. Large-scale impact of CO<sub>2</sub> storage in deep saline aquifers: a sensitivity study on pressure response in stratified systems. *Int J Greenh Gas Con* 2009;3(2):181–94.
- [32] Bachu S, Gunter WD, Perkins EH. Aquifer disposal of CO<sub>2</sub>: hydrodynamic and mineral trapping. *Energy Convers Manage* 1994;35(4):269–79.
- [33] Doughty C. Investigation of CO<sub>2</sub> plume behaviour for a large-scale pilot test of geologic carbon storage in a saline formation. *Transp Porous Med* 2010;82(1):49–76.
- [34] Pruess K, Nordbotten J. Numerical simulation studies of the long-term evolution of a CO<sub>2</sub> plume in a saline aquifer with a sloping caprock. *Transp Porous Med* 2011;90(1):135–51.
- [35] Zhang W, Li Y, Omambia AN. Reactive transport modeling of effects of convective mixing on long-term CO<sub>2</sub> geological storage in deep saline formations. *Int J Greenh Gas Con* 2011;5(2):241–56.
- [36] Helmig R. Multiphase flow and transport processes in the subsurface: a contribution to the modeling of hydrosystems. Berlin: Springer; 1997.
- [37] Jacob B. Dynamics of fluids in porous media. New York: McGraw-Hill; 1972.
- [38] Battistelli A, Calore C, Pruess K. The simulator TOUGH2/EWASG for modelling geothermal reservoirs with brines and non-condensable gas. *Geothermics* 1997;26(4):437–64.
- [39] García J. Density of aqueous solutions of CO<sub>2</sub>. Technical report LBNL-49023. Lawrence Berkeley National Laboratory, California; 2001.
- [40] Pruess K, Müller N. Formation dry-out from CO<sub>2</sub> injection into saline aquifers: 1. Effects of solids precipitation and their mitigation. *Water Resour Res* 2009;45:W03402.
- [41] Spycher N, Pruess K, Ennis-King J. CO<sub>2</sub>–H<sub>2</sub>O mixtures in the geological sequestration of CO<sub>2</sub>. I. Assessment and calculation of mutual solubilities from 12 to 100 °C and up to 600 bar. *Geochim Cosmochim Acta* 2003;67(16):3015–31.